



Cite as
Nano-Micro Lett.
(2023) 15:155

Received: 6 April 2023
Accepted: 14 May 2023
© The Author(s) 2023

Heteroatom-Induced Accelerated Kinetics on Nickel Selenide for Highly Efficient Hydrazine-Assisted Water Splitting and Zn-Hydrazine Battery

Hao-Yu Wang¹, Lei Wang¹, Jin-Tao Ren¹, Wen-Wen Tian¹, Ming-Lei Sun¹,
Zhong-Yong Yuan^{1,2} ✉

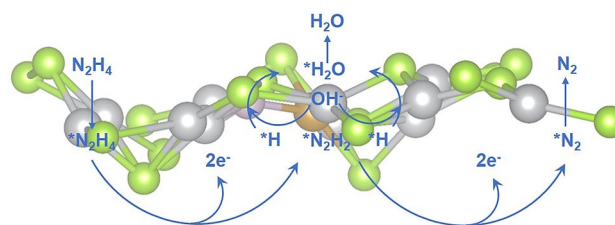
HIGHLIGHTS

- Ultrathin P and Fe co-doped NiSe₂ nanosheets supported on modified Ni foam are synthesized, which shows desirable bifunctional electrocatalytic hydrogen evolution reaction (HER)/hydrazine oxidation reaction (HzOR) performance in hydrazine-assisted water electrolysis and Zn-Hz battery.
- The coexistence of P and Fe heteroatoms induces an accelerated “2 + 2” reaction mechanism with a two-step HER process and a two-step HzOR step.

ABSTRACT

Hydrazine-assisted water electrolysis is a promising energy conversion technology for highly efficient hydrogen production. Rational design of bifunctional electrocatalysts, which can simultaneously accelerate hydrogen evolution reaction (HER)/hydrazine oxidation reaction (HzOR) kinetics, is the key step. Herein, we demonstrate the development of ultrathin P/Fe co-doped NiSe₂ nanosheets supported on modified Ni foam (P/Fe-NiSe₂) synthesized through a facile electrodeposition process and subsequent heat treatment. Based on electrochemical measurements, characterizations, and density functional theory calculations, a favorable “2 + 2” reaction mechanism with a two-step HER process and a two-step HzOR step was fully proved and the specific effect of P doping on HzOR kinetics was investigated. P/Fe-NiSe₂ thus yields an impressive electrocatalytic performance, delivering a high current density of 100 mA cm⁻² with potentials of -168 and 200 mV for HER and HzOR, respectively. Additionally, P/Fe-NiSe₂ can work efficiently for hydrazine-assisted water electrolysis and Zn-Hydrazine (Zn-Hz) battery, making it promising for practical application.

KEYWORDS Water electrolysis; Hydrogen production; Hydrazine oxidation; Bifunctional electrocatalyst; Heteroatom doping



✉ Zhong-Yong Yuan, zyyuan@nankai.edu.cn

¹ School of Materials Science and Engineering, Smart Sensing Interdisciplinary Science Center, Nankai University, Tianjin 300350, People's Republic of China

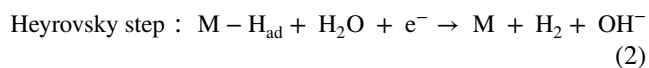
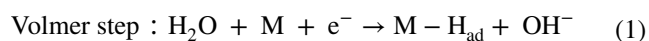
² Key Laboratory of Advanced Energy Materials Chemistry (Ministry of Education), Nankai University, Tianjin 300071, People's Republic of China



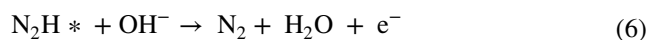
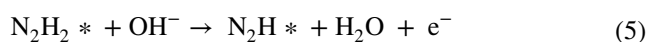
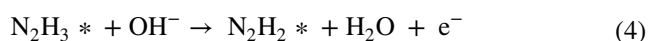
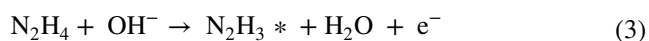
1 Introduction

Among various substitutes for fossil fuels, hydrogen, a green, clean and renewable energy resource with high gravimetric energy density, is considered as one of the most promising alternatives [1, 2]. Electrocatalytic water splitting is a promising pathway for the production of high-purity hydrogen with zero carbon emission [3–8]. Since oxygen evolution reaction (OER) with high thermodynamic oxidation potential and complex four-electron transfer process is unbenefiting and obstructive in practical application, various small molecules can participate into the oxidation process at the anode to replace sluggish OER process, such as hydrazine, ammonia, urea, methanol and ethanol [9–11]. Among them, hydrazine oxidation reaction (HzOR) with a high theoretical working potential advantage of 1.56 V compared with OER (OER: 1.23 V vs. RHE; HzOR: –0.33 V vs. RHE) can be a promising alternative [12]. Integrating cathodic hydrogen evolution reaction (HER) process and anodic HzOR process to construct a hydrazine-assisted water electrolyzer can efficiently decrease the applied cell voltage and avoid the mixing of anodic O₂ and cathodic H₂ in membrane-free devices [13].

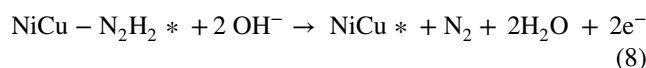
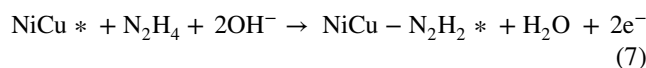
To simultaneously accelerate the reaction kinetics of both HER and HzOR, several properties should be given to electrocatalysts. In terms of HER process, non-noble metal electrocatalysts generally catalyze a Volmer–Heyrovsky mechanism in alkaline media [14–16]:



Herein, M and H_{ad} are the surface active sites and the adsorbed hydrogen, respectively. The sluggish dissociation process of water molecule and adsorption of H in Volmer step makes it the rate-determining step (RDS) in HER process. Consequently, efficient HER electrocatalyst should possess both the abilities to dissociate water molecules and adsorb H on the surface active sites. On the other hand, HzOR under alkaline conditions is a four-electron transfer process [17–19]:



Several intermediates and products are involved in the protonation processes of N₂H₄. Efficient HzOR electrocatalysts are required to have the ability to properly adsorb hydrazine molecules and promote the four consecutive deprotonation steps. Differently, an accelerated two-step HzOR mechanism was also proposed [20]. For example, Sun et al. concluded the HzOR mechanism on the Cu-doped Ni arrays [21]:



A former slow two-electron transfer process to produce diazene intermediate and a latter fast two-electron transfer process to generate N₂ are involved in this mechanism. However, a sufficient demonstration with corresponding characterization and electrochemical/calculation results of two-step HzOR mechanism has not been made so far, and the related parameters that can promote this two-step HzOR mechanism have not been discussed.

Recently, many Ni-based electrocatalysts are reported to exhibit excellent HER or HzOR electrocatalytic performance [22–26]. Among them, nickel selenide is promising to show bifunctional electrocatalytic activities on account of several electronic properties, including attraction of protons on the negatively charged Se atoms, favored hydrogen desorption by the weaker Se–H bonds and optimal adsorption N₂H_y intermediates to promote the deprotonation processes in HzOR [27, 28]. Nevertheless, single-component nickel selenide generally exhibits undesirable electrocatalytic performance, let alone simultaneously accelerating complex reaction kinetics of both HER and HzOR. Heteroatom doping is one of the most effective strategies to improve the electrocatalytic performance of catalysts [29, 30]. The doping metal and non-metal heteroatoms can introduce atomic distortions, tune the lattice/electronic structure and create additionally exposed active sites for different electrocatalytic reactions. The adsorption energy for different reaction intermediates can be thus optimized to accelerate reaction kinetics. P-doping is reported to tune the electronic structure of nickel selenide and reduce the energy barrier for HER and anodic oxidation reaction [31]. Besides, metal atom-doping, especially Fe-doping, is reported to accelerate electron transfer in electrocatalytic reactions, thus accelerating reaction kinetics compared with the un-doped counterparts [32, 33]. Based on the above considerations, we developed ultrathin P/Fe co-doped NiSe₂ nanosheets supported on modified Ni foam

(P/Fe-NiSe₂) synthesized through a two-step electrodeposition and subsequent selenization/phosphorous doping process. The as-synthesized electrocatalyst can thus catalyze favorable reaction kinetics for hydrazine-assisted water splitting. Low potentials of -168 and 200 mV are required to reach 100 mA cm^{-2} for HER and HzOR, respectively. More importantly, based on electrochemical measurements, characterizations and density functional theory (DFT) calculations, a favorable “2+2” reaction mechanism with a two-step HER process and a two-step HzOR step on P/Fe-NiSe₂ were fully proved, and the specific effect of P-doping on HzOR kinetics was investigated.

2 Experimental Section

2.1 Synthesis Procedures

Typically, a piece of commercial Ni foam (NF, $1 \text{ cm} \times 2 \text{ cm}$) was ultrasonically cleaned in hydrochloric acid, acetone, ethanol and deionized water to remove surface oxides and dried at 60°C prior to the synthesis process. Then, a two-step galvanostatic electrodeposition was carried out in a two-electrode system using the pretreated NF as the working electrode and a Pt wire as the counter electrode. In the first step, $0.1 \text{ M NiCl}_2 \cdot 6\text{H}_2\text{O}$ and $2 \text{ M NH}_4\text{Cl}$ were added in to the electrolyte solution, and a cathode current density of 1 A cm^{-2} was applied for 10 min . The NF modified with Ni microspheres was obtained. In the second step, $0.75 \text{ M Ni(NO}_3)_2 \cdot 6\text{H}_2\text{O}$ and $0.25 \text{ M FeSO}_4 \cdot 7\text{H}_2\text{O}$ were added in to the electrolyte solution and a cathodic current density of 10 mA cm^{-2} was applied for 200 s . The electrolyte solution was previously purged with N_2 for 30 min to avoid the oxidation of iron salts. After each electrodeposition process, the prepared sample was rinsed with deionized water and dried at room temperature. The obtained Fe-doped NiOH supported on NF was named as Fe-NiOH. The Fe-NiOH was then heated at 300°C for 90 min under N_2 flow with 200 mg powder selenide and $100 \text{ mg NaH}_2\text{PO}_2 \cdot \text{H}_2\text{O}$ placed near the Fe-NiOH at the upstream side to obtain the final product P/Fe co-doped NiSe₂ nanosheets supported on modified Ni foam (P/Fe-NiSe₂). By adjusting the pyrolyzation temperature from 300 to 250 and 200°C , P/Fe-NiSe₂-250 and P/Fe-NiSe₂-350 was obtained, respectively. For comparison, Fe-doped NiSe₂ nanosheets supported on modified Ni foam (Fe-NiSe₂) was prepared through a similar process to that of P/Fe-NiSe₂ without the addition of $\text{NaH}_2\text{PO}_2 \cdot \text{H}_2\text{O}$ in the

pyrolyzation process. NiSe₂ nanosheets supported on modified Ni foam (NiSe₂) was prepared through a similar process to that of Fe-NiSe₂ without the addition of $\text{FeSO}_4 \cdot 7\text{H}_2\text{O}$ in the second electrodeposition step.

2.2 Characterization

The Rigaku SmartLab diffractometer equipped with Cu-K α radiation was utilized to collect the X-ray diffraction (XRD) patterns. Scanning electron microscopy (SEM, Jeol JSM-7800F) and transmission electron microscopy (TEM, Jeol JEM-2800) were employed to characterize the structure and morphology of the synthesized materials. Utilizing a monochromatic Al-K α X-ray resource, X-ray photoelectron spectroscopy (XPS) was conducted via a Thermo Scientific ECSALAB 250Xi spectrometer. An electrochemical Nicolet iS50 spectrometer, complete with a VeeMAX III variable angle specular reflectance accessory as well as an electrochemical reaction cell, was utilized to characterize the electrochemical *in situ* Fourier transform infrared (FT-IR) spectroscopy.

2.3 Electrochemical Measurements

A typical three-electrode system was employed to measure the prepared catalysts' electrochemical hydrogen evolution/hydrazine oxidation performance. Here, our prepared sample acted as the working electrode, a Hg/HgO electrode operated as the reference electrode, and a Pt wire was used as the counter electrode. On the other hand, the overall water/hydrazine splitting performance of the catalysts was assessed using a two-electrode setup where our prepared sample served as both the anode and cathode. In measuring hydrogen evolution/overall water splitting and hydrazine oxidation/overall hydrazine splitting, the electrolyte was 1.0 M KOH and $1.0 \text{ M KOH} + 0.7 \text{ M N}_2\text{H}_4$, respectively.

3 Results and Discussions

3.1 Material Synthesis and Characterization

The ultrathin P/Fe co-doped NiSe₂ nanosheets supported on modified Ni foam were synthesized through a two-step electrodeposition process and subsequent pyrolysis process

for selenization and phosphorous doping, as shown in Scheme S1. In order to increase the roughness of NF and expose more active sites, the commercial NF with smooth surface (Fig. S1) was modified with Ni microspheres (Fig. S2) via a bubble template method in the first electrodeposition step (Fig. S3). Subsequently, ultrathin Fe-doped NiOH nanosheets were vertically grown on the surface of Ni microspheres during the second electrodeposition process (Fig. S4) to prepare the Fe-NiOH (Fig. S5). The as-prepared Fe-NiOH was then subjected to a low-temperature pyrolysis to simultaneously achieve selenization and phosphorous doping to obtain P/Fe-NiSe₂. For comparison, Fe-NiSe₂ and NiSe₂ were also prepared. The X-ray diffraction (XRD) patterns of P/Fe-NiSe₂ and Fe-NiSe₂ (Fig. 1a, b) show diffraction peaks indexed to NiSe₂ (PDF#41-1495), indicating that the original NiOH was transformed into NiSe₂ with P and Fe dopants (Fig. 1c). Scanning electron microscopy (SEM) images of P/Fe-NiSe₂ (Fig. 1d, f) show well retention of original morphology of Fe-NiOH after the selenization and P-doping during the pyrolysis process. Fe-NiSe₂ and NiSe₂ show similar morphology (Figs. S6 and S7), indicating that only composition differences exist between them. The high-resolution TEM image (Fig. 1g) shows the lattice fringes with interplanar spacing of 0.26 nm in the observational region, corresponding to NiSe₂ (2 1 0). Furthermore, the homogeneous distribution of doping P and Fe into the NiSe₂ lattice is demonstrated by scanning transmission electron microscopy (STEM) image and the corresponding elemental mappings of Ni, Fe, Se and P, proving the formation of P/Fe-co-doped NiSe₂ (Fig. 1h).

The elemental compositions and the effect of P/Fe-doping on the surface chemical states of P/Fe-NiSe₂ were investigated by X-ray photoelectron spectroscopy (Fig. 1i, j, k, l). The Ni 2*p* spectrum (Fig. 1i) of P/Fe-NiSe₂ shows two core-level peaks at 874.4 and 856.7 eV with their corresponding satellite peaks at 880.3 and 862.1 eV, which are ascribed to Ni²⁺ 2*p*_{1/2} and Ni²⁺ 2*p*_{3/2}, respectively [34]. Two peaks at 870.3 and 852.8 eV are assigned to the metallic state of Ni. Note that the binding energies of Ni 2*p*_{2/3} and the corresponding satellite peak of P/Fe-NiSe₂ exhibit an obviously positive shift of approximately 0.4 and 0.6 eV compared with Fe-NiSe₂ and NiSe₂, respectively. That indicates the positively charged metal atoms with decreased localization electron density [35]. By contrast, the Se 3*d* peak of P/Fe-NiSe₂ (Fig. 1j) at 54.4 eV shows negative shift compared with Fe-NiSe₂ and NiSe₂, indicating that Se atoms are

partially negatively charged after the incorporation of P and Fe atoms. These results demonstrate an electron distribution on Ni–Se bonds after heteroatom doping, contributing to decreased electron densities around Ni atoms and increased electron densities around Se atoms, which might optimize the adsorption of proton and hydrazine [36]. The other main peak in Se 3*d* spectrum at 58.7 eV is ascribed to Se–O bonding, which may be derived from surface oxidation of NiSe₂. The Fe 2*p* spectrums (Fig. 1k) of P/Fe-NiSe₂ and Fe-NiSe₂ show similar characteristic peaks of 2*p*_{1/2} (~723.6 eV) and 2*p*_{3/2} (~712.3 eV) and their corresponding satellite peaks at approximately 728.0 and 716.6 eV, respectively [37]. The P 2*p* spectrum (Fig. 1l) of P/Fe-NiSe₂ exhibits two main peaks at 130.3 and 134.3 eV, which are assigned to P 2*p* and P–O bonding, respectively [38]. Based on the aforementioned discussions, P and Fe atoms are successfully incorporated into the cubic NiSe₂ lattice to form P/Fe-co-doped ultrathin NiSe₂ nanosheets supported on modified Ni foam as a potential electrocatalyst for overall hydrazine splitting.

3.2 Electrochemical Measurements

Electrocatalytic HER and HzOR performances of the synthesized electrocatalysts were tested in a three-electrode system. First, linear sweep voltammetry (LSV) curves of P/Fe-NiSe₂ for HzOR in 1.0 M KOH with different hydrazine concentrations were compared to identify the optimum hydrazine concentration (Fig. S8). The reactive current densities obviously increase with N₂H₄ up to 0.7 M. Thus, the electrocatalytic HzOR performance of the synthesized electrocatalysts was all tested in 1.0 M KOH with addition of 0.7 M N₂H₄. In order to optimize the electrocatalytic performances for overall hydrazine splitting, the samples of P/Fe-NiSe₂-250 and P/Fe-NiSe₂-350 varying pyrolysis temperature to 250 and 350 °C were also synthesized and evaluated. Figure S9 shows that P/Fe-NiSe₂ employing 300 °C as the pyrolysis temperature exhibits the best bifunctional HER/HzOR performance. Therefore, P/Fe-NiSe₂ with the optimal synthesis condition was used in all the subsequent electrochemical measurements.

Figure 3a shows the LSV curves of P/Fe-NiSe₂ and other comparison samples Fe-NiSe₂, NiSe₂, bare NF and commercial Pt/C on NF for HER. P/Fe-NiSe₂ exhibits obviously enhanced electrocatalytic HER activity with decreased onset overpotential and increased current densities. The

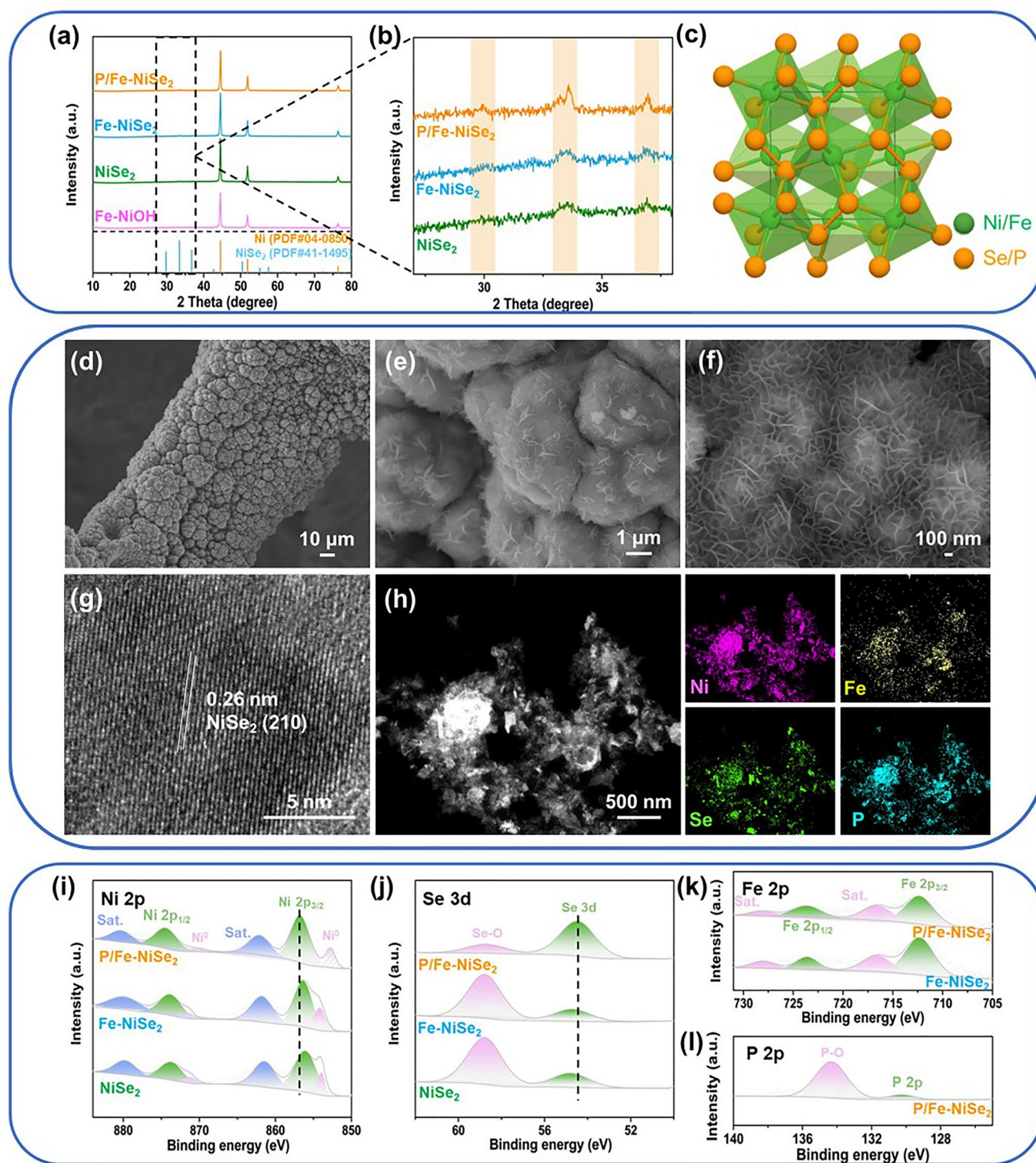


Fig. 1 a XRD patterns of P/Fe-NiSe₂, Fe-NiSe₂, NiSe₂ and Fe-NiOH. b Enlarged XRD patterns of P/Fe-NiSe₂, Fe-NiSe₂, NiSe₂ from 27 to 38 degree. c Crystal structure of P/Fe-NiSe₂. d-f SEM images of P/Fe-NiSe₂. g High-resolution TEM image of P/Fe-NiSe₂. h STEM image and the corresponding Ni, Fe, Se, P elemental mappings of P/Fe-NiSe₂. XPS characterization. i Ni 2p and j Se 3d of P/Fe-NiSe₂, Fe-NiSe₂ and NiSe₂. k Fe 2p of P/Fe-NiSe₂ and Fe-NiSe₂. l P 2p of P/Fe-NiSe₂

overpotential required for current density of 10 mA cm^{-2} is only 74 mV, which is superior to those of Fe-NiSe₂ (110 mV), NiSe₂ (141 mV), bare NF (230 mV) and slightly higher than that of commercial Pt/C (31 mV). This value of 74 mV is also lower than those of many recently reported efficient electrocatalysts (Fig. S10 and Table S1). The corresponding Tafel slope of P/Fe-NiSe₂, Fe-NiSe₂, and NiSe₂ is 49.3, 78.4 and 80.5 mV dec⁻¹, respectively, indicating faster reaction kinetics on P/Fe-NiSe₂ for rapid hydrogen evolution (Fig. 3b). By measuring cyclic voltammograms (CVs) at different scan rates (Fig. S11), the double-layer capacitance (C_{dl}) of P/Fe-NiSe₂ is calculated to be 77.7 mF cm^{-2} , which is close to those of Fe-NiSe₂ (66.1 mF cm^{-2}) and NiSe₂ (59.3 mF cm^{-2}) and much higher than that of pristine Ni foam (1.9 mF cm^{-2}), suggesting that more active sites can be exposed. The polarization curves using ECSA-normalized current densities (Fig. S13) reveal the intrinsic optimization of electrocatalytic active sites on P/Fe-NiSe₂ with P and Fe doping. Besides, the H₂ turn over frequency (TOF) per surface site was also calculated to further investigate the intrinsic HER activities of these electrocatalysts. The calculated TOFs are plotted against potential in Fig. S14. The TOF values for P/Fe-NiSe₂ are averagely more than 5 times larger than those for Fe-NiSe₂ and NiSe₂. Specifically, the experimental TOFs of P/Fe-NiSe₂, Fe-NiSe₂ and NiSe₂ are 4.5, 2.4 and 1.3 s⁻¹ at -0.1 V vs. RHE, respectively. These observations suggest that P/Fe-NiSe₂ possesses enhanced HER activity, which is mainly attributed to intrinsically optimized active sites with favorable reaction kinetics, rather than different active surface areas. The long-term stability of P/Fe-NiSe₂ was also evaluated by amperometry curves at a constant applied potential (Fig. 2c). The P/Fe-NiSe₂ can reserve the original current density of 100 mA cm^{-2} for over 24 h with less than 5% loss of current density. The LSV plots measured after stability test further demonstrate nearly unchanged electrocatalytic HER activity (inset Fig. 2c). In addition, the post-HER P/Fe-NiSe₂ were also investigated by SEM (Fig. S15), XRD (Fig. S16) and XPS analysis (Fig. S17), showing well retention of structure and composition with negligible change.

In addition to the excellent electrocatalytic HER performance, P/Fe-NiSe₂ also exhibits outstanding electrochemical HzOR performance in N₂H₄-containing 1.0 M KOH. As shown in the polarization curves in Fig. 2d, the P/Fe-NiSe₂ shows the best electrocatalytic HzOR performance with advantageous overpotentials and enhanced reactive current

densities. Specifically, the P/Fe-NiSe₂ can accomplish a current density of 100 mA cm^{-2} at a low potential of 200 mV, which makes it superior to Fe-NiSe₂ (294 mV), NiSe₂ (493 mV), commercial Pt/C catalyst and other recently reported efficient HzOR electrocatalysts (Fig. S10 and Table S2). As shown in Fig. 2e, P/Fe-NiSe₂ shows the smallest Tafel slope of 54.2 mV dec⁻¹, indicating an effective kinetical improvement after heteroatom doping, compared with Fe-NiSe₂ (78.4 mV dec⁻¹) and NiSe₂ (80.5 mV dec⁻¹). The ECSA-normalized polarization curves of different samples for HzOR are shown in Fig. S18. It can be observed that P/Fe-NiSe₂ shows lower overpotentials to obtain different current densities than Fe-NiSe₂ and NiSe₂, revealing intrinsically enhanced HzOR activity of P/Fe-NiSe₂. The electrochemical stability for HzOR is a crucial index to assess the performance of electrocatalysts. The long-term stability of P/Fe-NiSe₂ was evaluated by an amperometry test at a fixed potential. As shown in Fig. 2f, P/Fe-NiSe₂ can sustain a high current density of 100 mA cm^{-2} for over 24 h with minimal loss of current density and shows a good LSV overlapping with no obvious performance decay before and after the long-term stability test (inset Fig. 2f). Furthermore, the SEM (Fig. S19) and XRD (Fig. S20) analysis of the post-HzOR sample demonstrates respectable preservation of original morphology and crystallinity. In another concern, XPS analysis of P/Fe-NiSe₂ shows some modification after long-term HzOR stability test (Fig. S21). Specifically, the high-resolution Ni 2p XPS spectrum of post-HzOR P/Fe-NiSe₂ sample (Fig. S21a) shows the disappearance of characteristic peaks assigned to metallic Ni and Se 3d spectrum (Fig. S21b) shows an intensity increase at 58.7 eV (assigned to Se-O), which can be attributed to the partial oxidation of NiSe₂ during HzOR process. No other changes of structure can be detected on the post-HzOR P/Fe-NiSe₂, indicating the satisfactory stability of the electrode.

3.3 Overall Hydrazine Splitting and Zn-Hz Battery Performance

Considering the excellent electrocatalytic HER and HzOR performance of P/Fe-NiSe₂, is promising in overall hydrazine splitting (OH₂S) and other efficient devices (Fig. 3a). As shown in Fig. 3b, ultralow potentials are required for high current densities for hydrazine-assisted water electrolysis

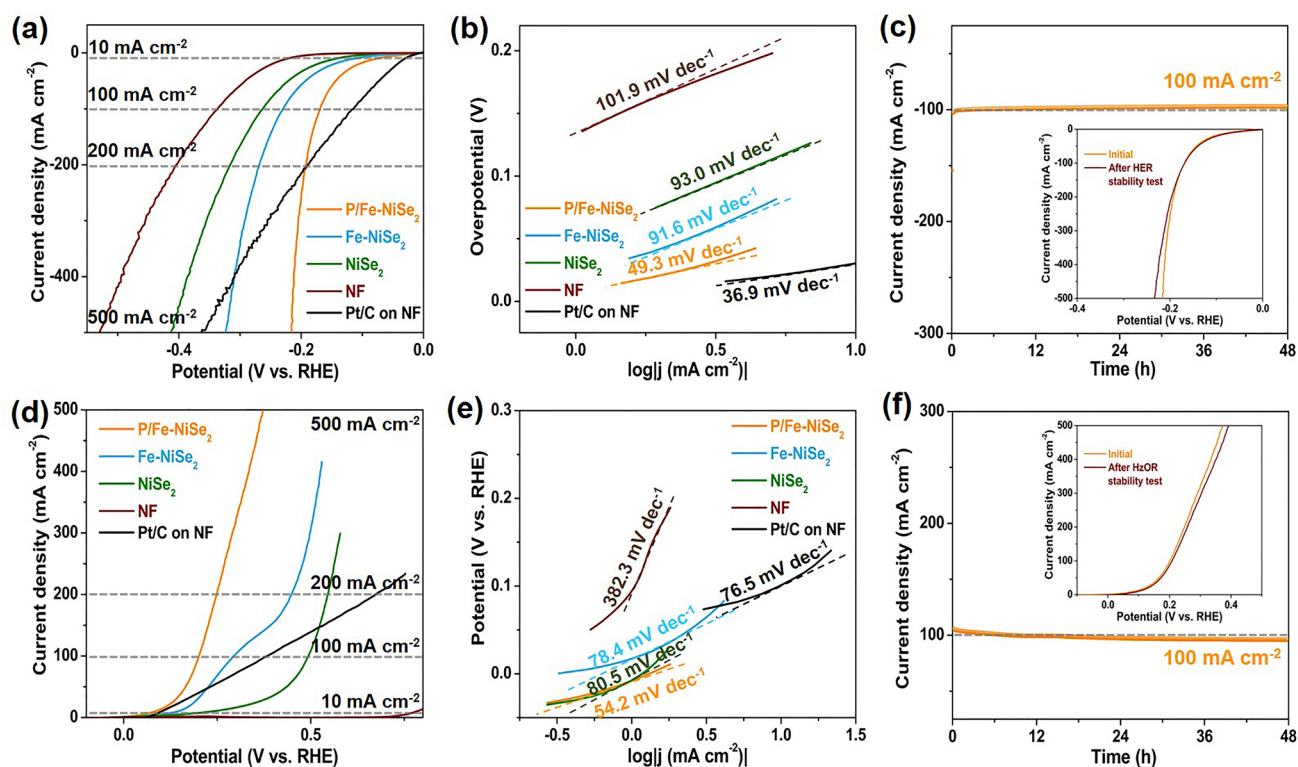


Fig. 2 Electrochemical hydrogen evolution/hydrazine oxidation performances of P/Fe-NiSe₂ and other comparison samples Fe-NiSe₂, NiSe₂, NF and Pt/C on NF. **a** Polarization curves for HER and corresponding **b** Tafel plots. **c** Amperometry for HER stability of P/Fe-NiSe₂. Inset: LSV measurement before and after HER stability test. **d** Polarization curves for HzOR and corresponding **e** Tafel plots. **f** Amperometry for HzOR stability of P/Fe-NiSe₂. Inset: LSV measurement before and after HzOR stability test

with decreased applied voltages of about 1.3 V compared with traditional water electrolysis, which could be powered by a commercial solar panel without additional applied potential under sunlight (Fig. S22). This electrolysis performance is better than that of many other recently reported electrocatalysts (Table S3). In addition, the OHZS device shows remarkably stable performance at a high current density of 100 mA cm⁻² for at least 100 h with negligible fluctuation of applied voltages (Fig. 3c). The faradaic efficiency was demonstrated to be approximately 100%, proving a high selectivity of P/Fe-NiSe₂ in hydrazine-assisted water electrolysis (Fig. S23). Zn-hydrazine (Zn-Hz) battery is a recently reported hydrazine-assisted energy conversion device, which is assembled with Zn foil as anode and bifunctional HER/HzOR electrocatalyst as cathode, separated by anion-exchange membrane (AEM) as separator [39]. At the anode, electrons transfer with the cycle of metal Zn and Zn(OH)₄²⁻. At the cathode, hydrogen is produced by the electrocatalytic HER during the discharge process, while nitrogen is produced through the electro-oxidation

of hydrazine during the charge process. As shown in Fig. S24, P/Fe-NiSe₂-assembled Zn-Hz battery could maintain an open circuit voltage of 0.330 V for more than 1 h, proving the feasibility in Zn-Hz battery. Figure 3d shows the discharge and charge polarization curves with small voltage gaps, further verifying the good feasibility. Figure 3e shows that the Zn-Hz battery could discharge stably at various current densities, especially at a relatively high current density of 20 mA cm⁻². The Zn-Hz battery could charge after long-term discharging, suggesting its good rechargeability. Based on the discharge voltage of 327 mV and the charge voltage of 337 mV at 0.4 mA cm⁻², the energy efficiency of this assembled Zn-Hz battery can be calculated to be more than 97%. Besides, the assembled Zn-Hz battery could operate stably for more than 300 cycles (100 h) at 5 mA cm⁻² without obvious voltage gap change, proving its excellent stability in the applied environment (Fig. S25). Thus, the P/Fe-NiSe₂-assembled Zn-Hz battery is promising to be a transfer station between intermittent renewable energy and P/Fe-NiSe₂-assembled water electrolyzer (Fig. 3a). The

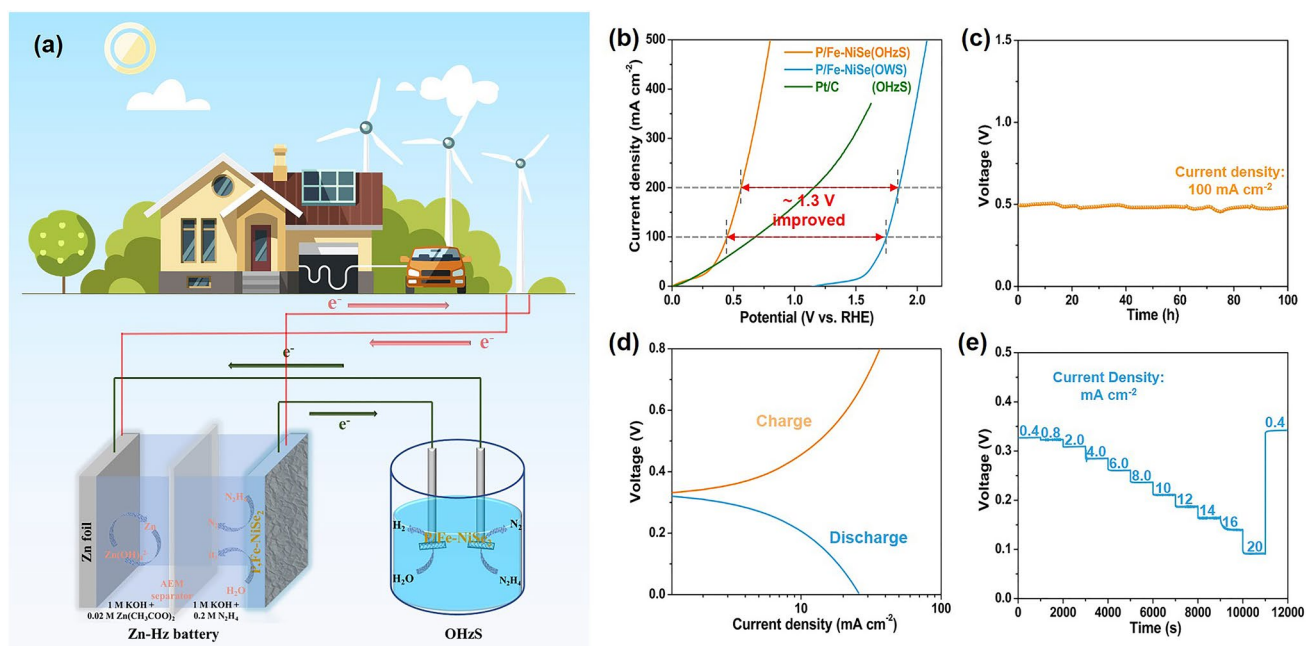


Fig. 3 **a** Schematic illustration of the combination of OH₂S, Zn-Hz battery and renewable energy. **b** Polarization curves for hydrazine-assisted water electrolysis. **c** Long-term stability test at a fixed current density of 100 mA cm⁻². **d** Polarization curves and **e** galvanostatic discharge/charge curves at different current densities for Zn-Hz battery

intermittent renewable energy like wind and solar energy can be stored in Zn-Hz battery to sustain the stable operation of water electrolysis device, which has great value in practical application.

3.4 Insight into the Accelerated Kinetics

Given the desirable bifunctional electrocatalytic performance, we applied further electrochemical analysis, characterization and theoretical calculation to investigate the favorable reaction kinetics of P/Fe-NiSe₂. For HER, the electrochemical impedance spectroscopy (EIS) measurements (Fig. S26) show that the samples with Fe-doping feature drastic fast charge transfer relative to NiSe₂ with low charge transfer resistance (R_{ct}) (Fig. S27). The electron transfer and electrocatalytic kinetics during HER process were further explored by *Operando* EIS at different potentials (Fig. S28). As shown in Fig. S28a-c, the Nyquist spectra at the low potentials show infinite R_{ct} with nearly vertical lines. Evident semicircles arise at higher applied potentials, suggesting that the electrocatalytic HER has appeared. P/Fe-NiSe₂ exhibits lower applied potential for the appearance of evident semicircle than Fe-NiSe₂

and NiSe₂, which is in line with the lower overpotentials in polarization curves, indicating higher electrocatalytic HER activity of P/Fe-NiSe₂. In addition, the change of phase angle (degree) with frequency is shown in the Bode phase plots (Fig. S28d-f). It is reported that the peaks of phase angle at low-frequency area can be attributed to the reaction charge transfer at the interface, which can be inspection parameter of hydrogen evolution reaction kinetics [40, 41]. It can be observed that P/Fe-NiSe₂ and Fe-NiSe₂ show similar decrease tendency of phase angle, which is much quicker than that of NiSe₂ without Fe-doping, suggesting faster reaction charge transfer at the interface and accelerated HER kinetics because of Fe doping. Besides, the temperature-dependent kinetic analysis (Fig. S29) shows a lower apparent activation energy value of for P/Fe-NiSe₂ (38.9 kJ mol⁻¹) compared to those of Fe-NiSe₂ (68.3 kJ mol⁻¹) and NiSe₂ (74.9 kJ mol⁻¹), proving the optimization in enthalpy of hydrogen evolution process due to the introduction of P atoms, reducing the kinetic barrier for the HER intermediates and accelerating the hydrogen evolution process [42, 43]. In situ Fourier transform infrared (FTIR) spectroscopy was employed to further investigate the specific effect of P doping at the

molecular level. As shown in the absorbance spectra collected at -0.1 V vs. RHE (Fig. S30), the most prominent peak at around 1640 cm^{-1} (green area in Fig. S30) is assigned to the OH bending mode, which represents the change of OH^- concentration on the reaction interface related to the hydrogen evolution process [44–46]. The negative-going band for P/Fe-NiSe₂ is obviously more intense than those for Fe-NiSe₂ and NiSe₂, demonstrating the accelerated HER kinetics by incorporation of P element.

For HzOR, to prove the two-step reaction mechanism hypothesis and investigate the specific effect of P doping on the HzOR reaction kinetics, CV curves of P/Fe-NiSe₂ and Fe-NiSe₂ were measured in 10 mM N₂H₄-containing 1.0 M KOH varying scan rates from 10 to 90 mV s⁻¹ (Fig. 4a, b). It can be observed that the nickel hydroxide-relevant anodic peak and hydrazine oxidation peak appear. The nickel hydroxide-relevant anodic peak current densities (I_p) and hydrazine oxidation peak current densities (j_p) increase and show a well-linear relationship with the increasing square root of scan rate (Fig. 4c), which suggest a diffusion-controlled HzOR process at low N₂H₄ concentrations. Specifically, j_p and its peak potential (E_p) have a quantitative relationship with the square root of scan rate, which can be described by the following equations [21, 47]:

$$j_p = 3.01 \times 10^5 n[(1 - \alpha)n_\alpha]^{1/2} AD^{1/2} C v^{1/2} \quad (9)$$

$$E_p = [2.303RT/(1 - \alpha)n_\alpha F] \log v + K \quad (10)$$

Here, n is the total electron transfer number, α is the electron transfer coefficient, n_α is the electron transfer number in the rate-determining step, A is the electrode geometric area, D is the diffusion coefficient, C is the bulk hydrazine concentration and v is the scan rate. R , T , F and K are the gas constant ($8.314\text{ J K}^{-1}\text{ mol}^{-1}$), temperature, Faraday constant ($96,485\text{ C mol}^{-1}$) and the constant, respectively. In this way, n_α of P/Fe-NiSe₂ and Fe-NiSe₂ are calculated to be 2.01 (approximately equal to 2) and 1.49, respectively. Thus, the rate-determining step of HzOR process on P/Fe-NiSe₂ involves a two-electron transfer process to produce a diazene intermediate, while that on Fe-NiSe₂ involves a mixture of one-electron transfer process and two-electron transfer process. This

can well explain the accelerated HzOR reaction kinetics on P/Fe-NiSe₂, which may be attributed to the positively charged Ni sites with reduced energy barrier for the dehydrogenation process in HzOR [3]. In situ Fourier transform infrared (FTIR) spectroscopy was employed to further investigate the reaction kinetics on modified active sites with the incorporation of P at the molecular level. When employing in situ FTIR spectroscopy over P/Fe-NiSe₂ in N₂H₄-containing KOH solution at 0.2 V vs. RHE for 200 s, several peaks assigned to N₂H_y ($1 \leq y \leq 4$) intermediates for HzOR increase and finally reach a stable state, including N–H stretching at around 3280 cm^{-1} , H–N–H bending at around 1450 cm^{-1} and -NH₂ wagging at around 1280 cm^{-1} (Fig. 4d) [48–50]. As shown in Fig. 4e, the amounts of different HzOR reaction intermediates of P/Fe-NiSe₂ are higher than that of Fe-NiSe₂, further revealing the accelerated reaction kinetics over P/Fe-NiSe₂ with modified electronic structure of Ni sites by the introduction of P element. Notably, compared with other peaks, the -NH₂ wagging peaks of P/Fe-NiSe₂ and Fe-NiSe₂ show a smaller absorbance gap, which can be attributed to different reaction mechanisms, specifically, the lack of N₂H₃ intermediate in the two-step hydrazine oxidation process for P/Fe-NiSe₂.

To investigate the origins of the superior bifunctional activity of P/Fe-NiSe₂ and the specific effect of P doping on the HzOR reaction kinetics, density functional theory (DFT) calculations were further performed (Fig. S31). ΔG_{H^*} is generally considered as the key parameter to evaluate the electrocatalytic hydrogen evolution performance, and a near thermoneutral ΔG_{H^*} is favorable for the adsorption and desorption of hydrogen [3]. The Gibbs free energy of the adsorbed H* (ΔG_{H^*}) on P/Fe-NiSe₂ and Fe-NiSe₂ is 0.07 and -0.57 eV, respectively (Fig. 4f), indicating an optimized H bonding on P/Fe-NiSe₂. Furthermore, water adsorption on the electrocatalytic surface is also critical for HER. A lower water adsorption energy ($\Delta E_{\text{H}_2\text{O}}$) on P/Fe-NiSe₂ was calculated to be -0.55 eV, compared with that of -0.32 eV on Fe-NiSe₂ (Fig. 4g), proving an accelerated water adsorption process on P/Fe-NiSe₂. For HzOR, the electrocatalytic performance depends on the free energies of each reaction intermediates in consecutive dehydrogenation steps. Figure 4h and Table S4 show the calculated Gibbs free energies for HzOR intermediates on P/Fe-NiSe₂. The solid line and the dotted line represent the traditional four-step and the suggested two-step HzOR process, respectively.

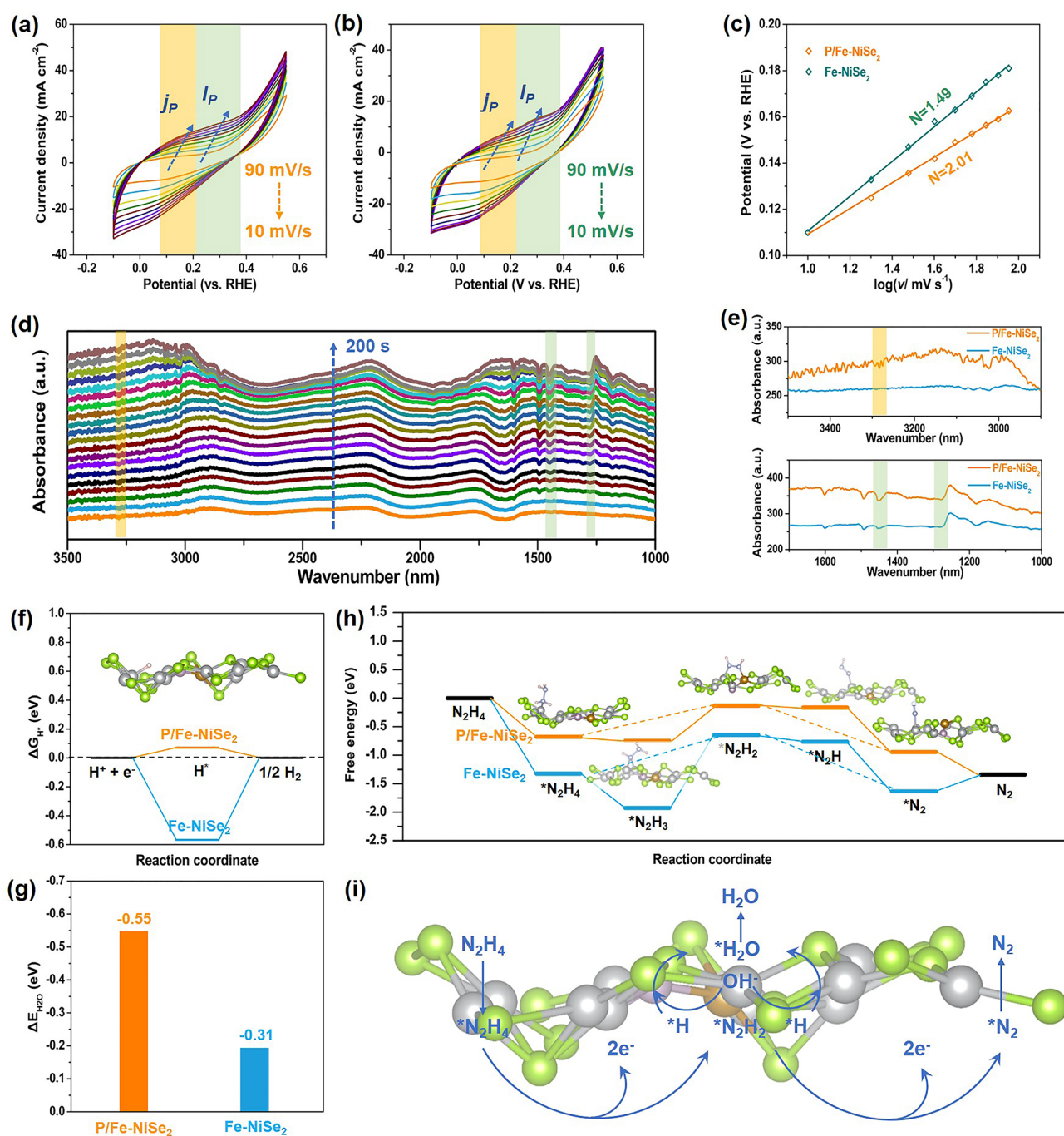


Fig. 4 CVs obtained with 10 mM hydrazine in 1.0 M KOH at different scan rates over **a** P/Fe-NiSe₂ and **b** Fe-NiSe₂. **c** HzOR peak potential plots versus $\log(v)$. **d**, **e** Electrochemical in situ FTIR spectroscopy over P/Fe-NiSe₂ and Fe-NiSe₂ for HzOR. **f** Gibbs free energy diagram for H adsorption. **g** H₂O adsorption energy. **h** Gibbs energy profiles for HzOR intermediates and the most stable configurations of each adsorbed intermediate for P/Fe-NiSe₂. **i** Schematic illustration of the proposed HzOR processes over P/Fe-NiSe₂

In terms of the four-step dehydrogenation process, the RDS for both P/Fe-NiSe₂ and Fe-NiSe₂ is the dehydrogenation from $*N_2H_3$ to $*N_2H_2$, in which the free energy difference

value for P/Fe-NiSe₂ (0.62 eV) is lower than that for Fe-NiSe₂ (1.28 eV), proving an accelerated hydrazine oxidation process on P/Fe-NiSe₂. Specifically, the free energy

difference value between the first and the second dehydrogenation process is relatively high (1.89 eV), indicating that the electro-oxidation of hydrazine on Fe-NiSe₂ involves a former fast electron transfer process to produce *N₂H₃ and a latter low electron transfer process to produce *N₂H₂, which is consistent with the FTIR results. Additionally, the free energy difference between the first dehydrogenation process and the two-electron process to produce *N₂H₂ is also high (1.28 eV), proving that the two-electron transfer process is relatively unfavored on Fe-NiSe₂. On the contrast, after P doping, these two free energy difference values dramatically decrease to be 0.69 and 0.62 eV, indicating a favored two-electron transferred process from *N₂H₄ to *N₂H₂ over P/Fe-NiSe₂. Similarly, the two-electron transferred process from *N₂H₂ to *N₂ is also preferable on P/Fe-NiSe₂, composing a two-step HzOR process, which can be illustrated by Fig. 4i. Thus, the bifunctional electrocatalytic HER and HzOR activity and a synthetically favorable “2 + 2” reaction mechanism with a two-step HER process and a two-step HzOR process of P/Fe-NiSe₂ have been proved, making it promising to be used in overall hydrazine splitting.

4 Conclusions

In summary, we have developed ultrathin P/Fe co-doped NiSe₂ nanosheets supported on modified Ni foam as highly efficient bifunctional HER and HzOR electrocatalysts for hydrazine-assisted water splitting. The prepared P/Fe-NiSe₂ can achieve a high current density of 100 mA cm⁻² at potentials of -168 and 200 mV for HER and HzOR, respectively. The specific effects of P and Fe doping have been investigated in view of accelerated charge transfer and optimized reaction kinetics based on electrochemical measurements, characterizations and DFT calculations. A favorable “2 + 2” reaction mechanism is thus concluded with a two-step HER process and a two-step HzOR step. This work not only reports an efficient bifunctional electrocatalyst for overall hydrazine splitting, but also provides a deeper mechanistic understanding of the heteroatom doping for HER/HzOR and may stimulate creativity for the development of advanced electrocatalysts for hydrogen production.

Acknowledgements This work was supported by the National Natural Science Foundation of China (22179065, 22111530112, 21875118), the Tianjin Graduate Research and Innovation Project

(2022BKY018) and the Ph.D. Candidate Research Innovation Fund of NKU School of Materials Science and Engineering.

Funding Open access funding provided by Shanghai Jiao Tong University.

Declarations

Conflict of interest The authors declare no interest conflict. They have no known competing financial interests or personal relationships that could have appeared to influence the work reported in this paper.

Open Access This article is licensed under a Creative Commons Attribution 4.0 International License, which permits use, sharing, adaptation, distribution and reproduction in any medium or format, as long as you give appropriate credit to the original author(s) and the source, provide a link to the Creative Commons licence, and indicate if changes were made. The images or other third party material in this article are included in the article's Creative Commons licence, unless indicated otherwise in a credit line to the material. If material is not included in the article's Creative Commons licence and your intended use is not permitted by statutory regulation or exceeds the permitted use, you will need to obtain permission directly from the copyright holder. To view a copy of this licence, visit <http://creativecommons.org/licenses/by/4.0/>.

Supplementary Information The online version contains supplementary material available at <https://doi.org/10.1007/s40820-023-01128-z>.

References

1. C. Dai, Y. Pan, B. Liu, Water splitting: conjugated polymer nanomaterials for solar water splitting. *Adv. Energy Mater.* **10**(42), 2070172 (2020). <https://doi.org/10.1002/aenm.202070172>
2. T. Gao, X. Tang, X. Li, S. Wu, S. Yu et al., Understanding the atomic and defective interface effect on ruthenium clusters for the hydrogen evolution reaction. *ACS Catal.* **13**(1), 49–59 (2023). <https://doi.org/10.1021/acscatal.2c04586>
3. Y. Zhu, J. Zhang, Q. Qian, Y. Li, Z. Li et al., Dual nanoislands on Ni/C hybrid nanosheet activate superior hydrazine oxidation-assisted high-efficiency H₂ production. *Angew. Chem. Int. Ed.* **61**(2), e202113082 (2022). <https://doi.org/10.1002/anie.202113082>
4. L.A. Zavala, K. Kumar, V. Martin, F. Maillard, F. Maugé et al., Direct evidence of the role of Co or Pt, Co single-atom promoters on the performance of MoS₂ nanoclusters for the hydrogen evolution reaction. *ACS Catal.* **13**(2), 1221–1229 (2023). <https://doi.org/10.1021/acscatal.2c05432>

5. G. Fu, X. Kang, Y. Zhang, X. Yang, L. Wang et al., Coordination effect-promoted durable Ni(OH)₂ for energy-saving hydrogen evolution from water/methanol Co-electrocatalysis. *Nano-Micro Lett.* **14**(1), 200 (2022). <https://doi.org/10.1007/s40820-022-00940-3>
6. Q. Xue, X.-Y. Bai, Y. Zhao, Y.-N. Li, T.-J. Wang et al., Au core-PtAu alloy shell nanowires for formic acid electrolysis. *J. Energy Chem.* **65**, 94–102 (2022). <https://doi.org/10.1016/j.jechem.2021.05.034>
7. Y. Liu, P. Vijayakumar, Q. Liu, T. Sakhivel, F. Chen et al., Shining light on anion-mixed nanocatalysts for efficient water electrolysis: fundamentals, progress, and perspectives. *Nano-Micro Lett.* **14**(1), 43 (2022). <https://doi.org/10.1007/s40820-021-00785-2>
8. Y. Ding, K.-W. Cao, J.-W. He, F.-M. Li, H. Huang et al., Nitrogen-doped graphene aerogel-supported ruthenium nanocrystals for pH-universal hydrogen evolution reaction. *Chinese J. Catal.* **43**(6), 1535–1543 (2022). [https://doi.org/10.1016/S1872-2067\(21\)63977-3](https://doi.org/10.1016/S1872-2067(21)63977-3)
9. H.-Y. Wang, M.-L. Sun, J.-T. Ren, Z.-Y. Yuan, Circumventing challenges: design of anodic electrocatalysts for hybrid water electrolysis systems. *Adv. Energy Mater.* **13**(4), 2203568 (2023). <https://doi.org/10.1002/aenm.202203568>
10. Y. Xue, Y. Guo, Q. Zhang, Z. Xie, J. Wei et al., MOF-derived Co and Fe species loaded on N-doped carbon networks as efficient oxygen electrocatalysts for Zn-air batteries. *Nano-Micro Lett.* **14**(1), 162 (2022). <https://doi.org/10.1007/s40820-022-00890-w>
11. J. Zhu, J. Qian, X. Peng, B. Xia, D. Gao, Etching-induced surface reconstruction of NiMoO₄ for oxygen evolution reaction. *Nano-Micro Lett.* **15**(1), 30 (2023). <https://doi.org/10.1007/s40820-022-01011-3>
12. Q. Qian, J. Zhang, J. Li, Y. Li, X. Jin et al., Artificial hetero-interfaces achieve delicate reaction kinetics towards hydrogen evolution and hydrazine oxidation catalysis. *Angew. Chem. Int. Ed.* **60**(11), 5984–5993 (2021). <https://doi.org/10.1002/anie.202014362>
13. Q. Sun, M. Zhou, Y. Shen, L. Wang, Y. Ma et al., Hierarchical nanoporous Ni(Cu) alloy anchored on amorphous NiFeP as efficient bifunctional electrocatalysts for hydrogen evolution and hydrazine oxidation. *J. Catal.* **373**, 180–189 (2019). <https://doi.org/10.1016/j.jcat.2019.03.039>
14. J. Li, J. Li, J. Ren, H. Hong, D. Liu et al., Electric-field-treated Ni/Co₃O₄ film as high-performance bifunctional electrocatalysts for efficient overall water splitting. *Nano-Micro Lett.* **14**(1), 148 (2022). <https://doi.org/10.1007/s40820-022-00889-3>
15. R. Li, H. Xu, P. Yang, D. Wang, Y. Li et al., Synergistic interfacial and doping engineering of heterostructured NiCo(OH)_x-Co_yW as an efficient alkaline hydrogen evolution electrocatalyst. *Nano-Micro Lett.* **13**(1), 120 (2021). <https://doi.org/10.1007/s40820-021-00639-x>
16. G. Qian, J. Chen, T. Yu, L. Luo, S. Yin, N-doped graphene-decorated NiCo alloy coupled with mesoporous NiCoMoO nano-sheet heterojunction for enhanced water electrolysis activity at high current density. *Nano-Micro Lett.* **13**(1), 77 (2021). <https://doi.org/10.1007/s40820-021-00607-5>
17. Y. Li, X. Yu, J. Gao, Y. Ma, Hierarchical Ni₂P/Zn–Ni–P nanosheet array for efficient energy-saving hydrogen evolution and hydrazine oxidation. *J. Mater. Chem. A* **11**(5), 2191–2202 (2023). <https://doi.org/10.1039/D2TA08366C>
18. Q. Yu, X. Liu, G. Liu, X. Wang, Z. Li et al., Constructing three-phase heterojunction with 1D/3D hierarchical structure as efficient trifunctional electrocatalyst in alkaline seawater. *Adv. Funct. Mater.* **32**(46), 2205767 (2022). <https://doi.org/10.1002/adfm.202205767>
19. X.-W. Lv, Q.-H. Kong, X.-L. Song, Y.-P. Liu, Z.-Y. Yuan, Coupling nonstoichiometric Cu_{2-x}Se with stable Cu₂Se berzelianite for efficient synergistic electrocatalytic hydrazine-assisted water splitting. *Inorg. Chem. Front.* **9**(23), 6182–6189 (2022). <https://doi.org/10.1039/D2QI01699K>
20. Y. Meng, X. Zou, X. Huang, A. Goswami, Z. Liu et al., Polypyrrole-derived nitrogen and oxygen co-doped mesoporous carbons as efficient metal-free electrocatalyst for hydrazine oxidation. *Adv. Mater.* **26**(37), 6510–6516 (2014). <https://doi.org/10.1002/adma.201401969>
21. Q. Sun, Y. Li, J. Wang, B. Cao, Y. Yu et al., Pulsed electro-deposition of well-ordered nanoporous Cu-doped Ni arrays promotes high-efficiency overall hydrazine splitting. *J. Mater. Chem. A* **8**(40), 21084–21093 (2020). <https://doi.org/10.1039/D0TA08078K>
22. F. Qin, Z. Zhao, M.K. Alam, Y. Ni, F. Robles-Hernandez et al., Trimetallic NiFeMo for overall electrochemical water splitting with a low cell voltage. *ACS Energy Lett.* **3**(3), 546–554 (2018). <https://doi.org/10.1021/acscenergylett.7b01335>
23. C. Zhu, Z. Yin, W. Lai, Y. Sun, L. Liu et al., Fe-Ni-Mo nitride porous nanotubes for full water splitting and Zn-air batteries. *Adv. Energy Mater.* **8**(36), 1802327 (2018). <https://doi.org/10.1002/aenm.201802327>
24. C. Tang, R. Zhang, W. Lu, Z. Wang, D. Liu et al., Energy-saving electrolytic hydrogen generation: Ni₂P nanoarray as a high-performance non-noble-metal electrocatalyst. *Angew. Chem. Int. Ed.* **56**(3), 842–846 (2017). <https://doi.org/10.1002/anie.201608899>
25. L. Hang, T. Zhang, D. Men, L. Liang, Y. Chen et al., Constructing nickel-based bifunctional oxygen catalyst and dual network hydrogel electrolyte for high-performance, compressible and rechargeable zinc-air batteries. *Mater. Today Phys.* **29**, 100924 (2022). <https://doi.org/10.1016/j.mtphys.2022.100924>
26. J. Zhou, L. Yu, Q. Zhou, C. Huang, Y. Zhang et al., Ultrafast fabrication of porous transition metal foams for efficient electrocatalytic water splitting. *Appl. Catal. B-Environ.* **288**, 120002 (2021). <https://doi.org/10.1016/j.apcatb.2021.120002>
27. X. Peng, Y. Yan, X. Jin, C. Huang, W. Jin et al., Recent advance and perspectives of electrocatalysts based on transition metal selenides for efficient water splitting. *Nano Energy* **78**, 105234 (2020). <https://doi.org/10.1016/j.nanoen.2020.105234>
28. X. Xia, L. Wang, N. Sui, V.L. Colvin, W.W. Yu, Recent progress in transition metal selenide electrocatalysts for water

- splitting. *Nanoscale* **12**(23), 12249–12262 (2020). <https://doi.org/10.1039/D0NR02939D>
29. Z. Wang, H. Liu, R. Ge, X. Ren, J. Ren et al., Phosphorus-doped Co_3O_4 nanowire array: a highly efficient bifunctional electrocatalyst for overall water splitting. *ACS Catal.* **8**(3), 2236–2241 (2018). <https://doi.org/10.1021/acscatal.7b03594>
30. C. Huang, J. Zhou, D. Duan, Q. Zhou, J. Wang et al., Roles of heteroatoms in electrocatalysts for alkaline water splitting: A review focusing on the reaction mechanism. *Chin. J. Catal.* **43**(8), 2091–2110 (2022). [https://doi.org/10.1016/S1872-2067\(21\)64052-4](https://doi.org/10.1016/S1872-2067(21)64052-4)
31. J. Yu, W.-J. Li, G. Kao, C.-Y. Xu, R. Chen et al., In-situ growth of CNTs encapsulating P-doped NiSe_2 nanoparticles on carbon framework as efficient bifunctional electrocatalyst for overall water splitting. *J. Energy Chem.* **60**, 111–120 (2021). <https://doi.org/10.1016/j.jechem.2020.12.030>
32. T. Wang, D. Gao, W. Xiao, P. Xi, D. Xue et al., Transition-metal-doped NiSe_2 nanosheets towards efficient hydrogen evolution reactions. *Nano Res.* **11**(11), 6051–6061 (2018). <https://doi.org/10.1007/s12274-018-2122-9>
33. C. Gu, S. Hu, X. Zheng, M.-R. Gao, Y.-R. Zheng et al., Synthesis of sub-2 nm iron-doped NiSe_2 nanowires and their surface-confined oxidation for oxygen evolution catalysis. *Angew. Chem. Int. Ed.* **57**(15), 4020–4024 (2018). <https://doi.org/10.1002/anie.201800883>
34. Y. Zhao, B. Jin, A. Vasileff, Y. Jiao, S.-Z. Qiao, Interfacial nickel nitride/sulfide as a bifunctional electrode for highly efficient overall water/seawater electrolysis. *J. Mater. Chem. A* **7**(14), 8117–8121 (2019). <https://doi.org/10.1039/C9TA01903K>
35. Y. Wu, X. Liu, D. Han, X. Song, L. Shi et al., Electron density modulation of NiCo_2S_4 nanowires by nitrogen incorporation for highly efficient hydrogen evolution catalysis. *Nat. Commun.* **9**(1), 1425 (2018). <https://doi.org/10.1038/s41467-018-03858-w>
36. Y. Pan, K. Sun, S. Liu, X. Cao, K. Wu et al., Core-shell ZIF-8@ZIF-67-derived CoP nanoparticle-embedded N-doped carbon nanotube hollow polyhedron for efficient overall water splitting. *J. Am. Chem. Soc.* **140**(7), 2610–2618 (2018). <https://doi.org/10.1021/jacs.7b12420>
37. H. Liang, A.N. Gandi, C. Xia, M.N. Hedhili, D.H. Anjum et al., Amorphous NiFe-OH/NiFeP electrocatalyst fabricated at low temperature for water oxidation applications. *ACS Energy Lett.* **2**(5), 1035–1042 (2017). <https://doi.org/10.1021/acsenergylett.7b00206>
38. L. Zeng, K. Sun, X. Wang, Y. Liu, Y. Pan et al., Three-dimensional-networked $\text{Ni}_2\text{P/Ni}_3\text{S}_2$ heteronanoflake arrays for highly enhanced electrochemical overall-water-splitting activity. *Nano Energy* **51**, 26–36 (2018). <https://doi.org/10.1016/j.nanoen.2018.06.048>
39. Y. Feng, Q. Shi, J. Lin, E. Chai, X. Zhang et al., Decoupled electrochemical hydrazine “splitting” via a rechargeable Zn-hydrazine battery. *Adv. Mater.* **34**(51), 2207747 (2022). <https://doi.org/10.1002/adma.202207747>
40. C. Xie, W. Chen, S. Du, D. Yan, Y. Zhang et al., In-situ phase transition of WO_3 boosting electron and hydrogen transfer for enhancing hydrogen evolution on Pt. *Nano Energy* **71**, 104653 (2020). <https://doi.org/10.1016/j.nanoen.2020.104653>
41. K. Gu, D. Wang, C. Xie, T. Wang, G. Huang et al., Defect-rich high-entropy oxide nanosheets for efficient 5-hydroxymethylfurfural electrooxidation. *Angew. Chem. Int. Ed.* **60**(37), 20253–20258 (2021). <https://doi.org/10.1002/anie.202107390>
42. Y. Duan, N. Dubouis, J. Huang, D.A. Dalla Corte, V. Pimenta et al., Revealing the impact of electrolyte composition for Co-based water oxidation catalysts by the study of reaction kinetics parameters. *ACS Catal.* **10**(7), 4160–4170 (2020). <https://doi.org/10.1021/acscatal.0c00490>
43. J. Huang, H. Sheng, R.D. Ross, J. Han, X. Wang et al., Modifying redox properties and local bonding of Co_3O_4 by CeO_2 enhances oxygen evolution catalysis in acid. *Nat. Commun.* **12**(1), 3036 (2021). <https://doi.org/10.1038/s41467-021-23390-8>
44. L. Wang, S. Zhu, N. Marinkovic, S. Kattel, M. Shao et al., Insight into the synergistic effect between nickel and tungsten carbide for catalyzing urea electrooxidation in alkaline electrolyte. *Appl. Catal. B-Environ.* **232**, 365–370 (2018). <https://doi.org/10.1016/j.apcatb.2018.03.064>
45. X.-W. Lv, W.-S. Xu, W.-W. Tian, H.-Y. Wang, Z.-Y. Yuan, Activity promotion of core and shell in multifunctional core-shell $\text{Co}_2\text{P@NC}$ electrocatalyst by secondary metal doping for water electrolysis and Zn-air batteries. *Small* **17**(38), 2101856 (2021). <https://doi.org/10.1002/smll.202101856>
46. H. Hanawa, K. Kunimatsu, M. Watanabe, H. Uchida, In situ ATR-FTIR analysis of the structure of Nafion–Pt/C and Nafion– $\text{Pt}_3\text{Co/C}$ interfaces in fuel cell. *J. Phys. Chem. C* **116**(40), 21401–21406 (2012). <https://doi.org/10.1021/jp306955q>
47. L.-X. Chen, L.-Y. Jiang, A.-J. Wang, Q.-Y. Chen, J.-J. Feng, Simple synthesis of bimetallic AuPd dendritic alloyed nanocrystals with enhanced electrocatalytic performance for hydrazine oxidation reaction. *Electrochim. Acta* **190**, 872–878 (2016). <https://doi.org/10.1016/j.electacta.2015.12.151>
48. Y. Yao, S. Zhu, H. Wang, H. Li, M. Shao, A spectroscopic study on the nitrogen electrochemical reduction reaction on gold and platinum surfaces. *J. Am. Chem. Soc.* **140**(4), 1496–1501 (2018). <https://doi.org/10.1021/jacs.7b12101>
49. X.-W. Lv, X.-L. Liu, Y.-J. Suo, Y.-P. Liu, Z.-Y. Yuan, Identifying the dominant role of pyridinic-N–Mo bonding in synergistic electrocatalysis for ambient nitrogen reduction. *ACS Nano* **15**(7), 12109–12118 (2021). <https://doi.org/10.1021/acsnano.1c03465>
50. H.-Y. Wang, J.-T. Ren, C.-C. Weng, X.-W. Lv, Z.-Y. Yuan, Insight into the valence state of sisal-like MoO_2 nanosheet arrays for N_2 electrolysis. *Chem. Eng. J.* **426**, 130761 (2021). <https://doi.org/10.1016/j.cej.2021.130761>

